PHYSICAL REVIEW A VOLUME 58, NUMBER 1 JULY 1998

Classical motion of a photoelectron interacting with its ionic core: Slow photoelectron imaging

Christian Bordas
Laboratoire de Spectrométrie Ionique et Moléculaire, UMR CNRS 5579, Université Claude Bernard, Lyon 1, Bâtiment 205,
43 Boulevard du 11 Novembre 1918, F69622 Villeurbanne Cedex, France

(Received 13 January 1998)

Photoelectron imaging spectroscopy relies on the properties of the ballistic trajectories of photoelectrons moving in a homogeneous electric field. In this paper we show that the simple picture of parabolic trajectories is no longer valid when slow photoelectrons produced in the vicinity of the zero-field ionization threshold, and especially just above the saddle-point energy, are concerned. The discussion presented here is based on the exact classical simulation of the trajectories of photoelectrons in the combined Coulomb and Stark field. It is shown that under rather common experimental conditions the influence of the Coulomb interaction on the projection pattern of photoelectrons at large distance is dramatic. In standard photoelectron imaging spectroscopy a single feature corresponds to a given ionization channel, while we show here that the observed features are much more complex for slow photoelectrons. We then discuss the relevance of our classical simulations as compared with wave-packet calculations. Finally, the application of this effect to the precise characterization of near-zero-energy resonance in atoms in external fields and to the dynamics of zero-kinetic-energy electrons is presented. [S1050-2947(98)09006-4]

PACS number(s): 32.60.+i, 32.80.Fb

I. INTRODUCTION

The study of the Stark effect in hydrogenic systems is one of the oldest problems in quantum mechanics [1]. The high degree of symmetry of the problem of one electron in the combined Coulomb and homogeneous Stark field allows an exact separation of the equations of motion in parabolic coordinates. This topic has been the subject of many theoretical papers, even in recent years [2–8]. Essentially, the Coulomb plus Stark problem contains many ingredients which makes it of universal interest. Among these ingredients, one of the most essential is that, strictly speaking, this problem does not possess any true discrete state owing to the divergence of the potential along the field direction. However, below the classical ionization limit, quasidiscrete states exist and many approaches have been used to calculate the Stark resonances, from low-lying states to very excited states, even above the zero-field ionization limit. One of the many reasons of the great interest in Stark effect is the extreme sensitivity of Rydberg states to external electric field [9]. This has generated a huge amount of literature in this field, both theoretical [2–8] and experimental [10–15]. Moreover in this area, the use of classical mechanics has been the basis of many interpretations for a long time. Indeed, since the electron motion is open in one direction, it is always relevant to discuss specific features of Stark spectra in comparison with classical trajectories. This approach has been very fruitful to analyze, in particular, the time evolution of the Rydberg states in the presence of a field [16–18] or the resonances above the ionization limit [19,20], signatures of quasiclosed classical orbits.

The understanding of the structure and dynamics of a simple nonhydrogenic quantum system in an external electric field is a fundamental problem relevant to various physical processes such as photoionization or Rydberg state spectroscopy. Of particular interest is the specific shape of the effective potential experienced by the external electron in the combination of the Coulomb and Stark field. It is well known that the shape of this potential, which presents a saddle point at energy $-\sqrt{2F}$, is responsible for the so-called field-induced ionization. The study of field-induced ionization has been the subject of many articles [21–24] and is directly at the origin of the ZEKE (zero-kinetic-energy) spectroscopy [25,26]. Moreover, in the vicinity of the saddle-point energy, the Coulomb plus Stark potential behaves like a bottleneck which strongly affects the classical trajectory of the electrons excited above the critical saddle-point energy. For example, in the pure Coulomb plus Stark field, even above the saddle-point energy, some classical trajectories are stable for certain initial conditions [19,20]. In a series of famous papers, Kondratovitch and Ostrovsky [27] have discussed the classical motion of electrons in a hydrogenic system in a static external field and have derived a semiclassical analysis of the quantum interferences which result from the coexistence of multiple trajectories leading to the same impact position. These papers are directly at the origin of the photodetachment microscope described recently by Blondel, Delsart, and Dulieu [28]. However, these concepts of microscopy and interferences are more relevant to the case where no long-range interaction affects the escaping electron: i.e., photodetachment. The principle of the photoelectron imaging spectrometry developed by Helm and co-workers [29–31] is also more or less contained in these papers. In this article we discuss more specifically the classical motion of slow electrons and we examine what can be learned from the geometrical patterns of electrons projected onto a position sensitive detector using the technique of photoelectron imaging spectroscopy. In particular, the connection between slow photoelectron imaging and continuum Stark spectroscopy [32–35] will be outlined.

The technique of photoelectron imaging spectroscopy [29–31] allows direct visualization on a position sensitive detector (PSD) of the initial velocity and the angular distribution of electrons emitted in a photoionization process. This technique is based on the following principle: electrons emitted at a given position with a kinetic energy W in a static field F detected on a PSD at a distance L from the origin give rise to a circular image of radius $R \approx 2L\sqrt{W/qFL}$ with a filling pattern that reveals the original angular distribution of the electrons. In a first approximation, the interaction of the photoelectron with its ionic core is neglected. This is realistic for the case of electrons of kinetic energy large enough (typically $W > 10$ meV). However, the Coulomb attraction between the electron and the ionic core cannot be neglected when slow (or ZEKE) electrons are concerned. In this paper we examine more carefully the classical trajectories of electrons emitted in the vicinity of the ionization threshold in weak electric field. From a classical point of view, the motion of an electron in the combination of a static plus a Coulomb field is, despite its relative simplicity, one of the most complex problems having exact analytical solutions. In the first section of this paper we present a reminder of the classical motion of the electron in the combined Coulomb and Stark field based on the results of Kondratovitch and Ostrovsky [27]. Beside the interference effects discussed by these authors, another property of the classical motion of slow electrons has not been addressed so far: namely, the influence of the Coulomb field of the residual ion on the pattern of impacts of slow electrons on a two-dimensional (2D) detector in a weak electric field. This aspect is discussed in the second section of this paper where we examine the breakdown of the ballistic approximation near the zero-field ionization threshold. It is shown that, at low initial kinetic energy, it is possible to obtain a photoelectron image displaying a complex structure which carries additional information on the initial velocity distribution, instead of the single ring expected for a single ionization channel. The relevance of our classical model in comparison with wave-packet quantum calculations [16,17] is then discussed. Beside the new approach of continuum Stark spectroscopy [32–35] provided by the effect described here, we demonstrate that photoelectron imaging at threshold provides a tool to discriminate between electrons emitted in various directions with respect to the laser polarization but also with respect to the external field, which has not been achieved up to now except indirectly in the time domain [17,36]. The last section is thus devoted to some of the many applications offered by this technique: direct visualization of the localization of the wave function for quasidiscrete resonances in the continuum, dynamics of photoionization, and finally the relevance of this phenomenon in the field of ZEKE spectroscopy and especially the influence of neighboring ions.

II. THE CLASSICAL ELECTRON MOTION

The technique of photoelectron imaging spectroscopy described in detail in Refs. [29–31] allows us to directly visualize the initial velocity and the angular distribution of electrons emitted in a photoionization process. In this method, electrons emitted at a given position with a kinetic energy W are projected by a homogeneous electric field $\mathbf{F}$ on a position sensitive detector (see Fig. 1). This results in an image which is the superposition of circular rings of radius $R_i \approx 2L\sqrt{W_i/qFL}$ for each energy channel W_i. The filling patterns of the various concentric rings reveal the original angular distribution of the electrons after inversion of the image by means of an Abel inversion. In the standard imaging technique [31], the interaction of the photoelectron with its ionic core is neglected. This is realistic for the case of electrons of kinetic energy large enough so that the Coulomb interaction which prevails on typical distances of a few micrometers is low as compared to the kinetic energy W. When this approximation holds, electrons follow simple ballistic (parabolic) trajectories and the coordinates of the impact on the detector can be derived using very simple algebra. Using the coordinate axis defined in Fig. 1, one finds

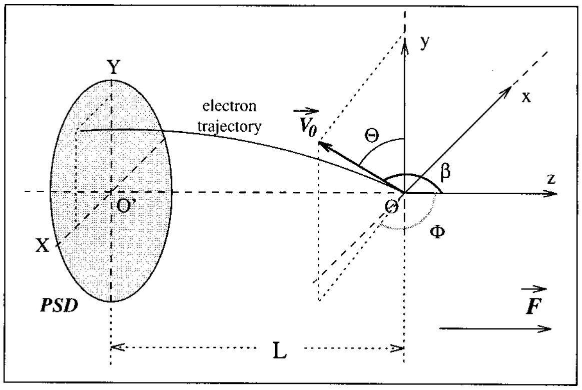

FIG. 1. Principle of the photoelectron imaging. The laser propagates along the O_x axis and is polarized along the O_y axis. The electric field $\mathbf{F}$ is oriented along the O_z axis. Θ is defined as the angle between the laser polarization and the initial velocity $\mathbf{v}_0$ of the photoelectron, while β is the angle between $\mathbf{v}_0$ and the external field $\mathbf{F}$.

$$X = \frac{2L\cos\Phi\sin\Theta}{\rho}\left(\sqrt{\sin^2\Phi\sin^2\Theta+\rho}-\sin\Phi\sin\Theta\right),$$

$$Y = \frac{2L\cos\Theta}{\rho}\left(\sqrt{\sin^2\Phi\sin^2\Theta+\rho}-\sin\Phi\sin\Theta\right), \quad (1)$$

where

$$\rho = \frac{qFL}{W_0} \quad (2)$$

is the ratio between the electrostatic energy accumulated in the external field F over a length L, and the initial kinetic energy W_0.

However, the Coulomb attraction between the electron and the ionic core can no longer be neglected when very slow electrons are concerned. In that case, the simple ballistic flight must be replaced by a more refined calculation allowing for both the electrostatic potential $(-qFz)$ and the Coulomb potential $(-q/r)$. The problem of an electron in the combination of a Coulomb and a Stark field has exact analytical solutions in classical mechanics. The nature of these solutions has been extensively studied by Beletzky [37] in the context of celestial mechanics. Similarly to the quantum problem, the equations of the classical motion are separable in parabolic coordinates ($\xi = r+z$; $\eta = r-z$; ϕ). But, as opposed to the quantum mechanics, the classical problem is fully integrable and has exact analytical solutions. Indeed, the presence of the infinite motion along the η coordinate prevents the existence of exact discrete states and, although the perturbation series may be calculated to an arbitrary precision [4] it leads to a numerical divergence of the series. The classical motion has been described thoroughly by Kondratovitch and Ostrovsky in Ref. [27]. Let us recall the main results of this analysis. Introducing the reduced time variable τ according to $d\tau = dt/r$ the equations of motion for an electron of total energy E (with respect to the zero-field ionization threshold) in a static field F become (in atomic units)

$$\frac{d\xi}{d\tau} = 2\xi\left(\frac{1}{2}E + \frac{Z_1}{\xi} - \frac{p_\phi^2}{4\xi^2} - \frac{1}{4}F\xi\right)^{1/2},$$

$$\frac{d\eta}{d\tau} = 2\eta\left(\frac{1}{2}E + \frac{Z_2}{\eta} - \frac{p_\phi^2}{4\eta^2} + \frac{1}{4}F\eta\right)^{1/2}. \tag{3}$$

Without lack of generality, let us focus our discussion on the case of the plane motion which is distinguished by the zero value of the orbital momentum p_ϕ on the field axis $\mathbf{F}$. The separation constants Z_1 and Z_2 ($Z_1 + Z_2 = Z$ atomic charge of the ion core) may be related to the ejection angle β between the initial velocity of the photoelectron and the field axis:

$$Z_1 = Z\cos^2(\beta/2), \quad Z_2 = Z\sin^2(\beta/2). \tag{4}$$

The integration of Eqs. (3) gives the parabolic coordinates ξ and η as a combination of the Jacobi elliptic functions of the reduced time variable τ.

(i) Motion along the ξ coordinate. Along this coordinate, the classical motion is periodic in τ and confined in a limited region. Depending on the initial conditions the electron may perform one or several oscillations (with N_ξ turning points) along the ξ axis before escaping:

$$\xi(\tau) = \frac{|\xi_-|\,\mathrm{sn}^2(\varphi|m_\xi)}{m_\xi^{-1} - \mathrm{sn}^2(\varphi|m_\xi)}, \tag{5a}$$

where

$$|\xi_-| = p\left[\left(1 + \frac{Z_1}{Z_c}\right)^{1/2} - \mathrm{sgn}(E)\right] \text{ and } p = \frac{|E|}{F}. \tag{5b}$$

The variable and argument of the elliptic sine function are defined as

$$\varphi = 2^{-1/2}\left(1 + \frac{Z_1}{Z_c}\right)^{1/4} x, \quad m_\xi = \frac{1}{2}\left[1 + \mathrm{sgn}(E)\left(1 + \frac{Z_1}{Z_c}\right)^{-1/2}\right], \tag{5c}$$

with

$$Z_c = \frac{E^2}{4F} \text{ and } x = |E|^{1/2}\tau. \tag{5d}$$

(ii) Motion along the η coordinate. Along η, the motion is either bound and no ionization occurs, or it is open and $\eta(\tau)$ increases monotonically with time. The nature of the motion along the η coordinate strongly depends on the relative position of the total energy E with respect to the saddle-point energy E_c defined as

$$E_c = -2\sqrt{ZF}. \tag{6}$$

Let us define the reduced energy ε as

$$\varepsilon = \frac{E}{|E_c|} = \mathrm{sgn}(E)\left(\frac{Z_c}{Z}\right)^{1/2}. \tag{7}$$

For $E \leqslant -2\sqrt{Z_2F}$ the electron motion is bound. In classical mechanics, the electron launched at an angle $\beta < \beta_c$ such that $E \leqslant -2\sqrt{Z_2F}$ can never escape the attraction field of its ion, even though its energy lies above the saddle point. The critical angle β_c is

$$\beta_c = 2\arcsin\left(\frac{-E}{2\sqrt{ZF}}\right). \tag{8}$$

The consequence of this classical feature in quantum mechanics is the longer lifetime of the blue Stark states (states whose energy increases with F) whose wave function is predominantly located in the upfield region. On the other hand, red Stark states, mostly localized in the downfield region, have a lifetime shorter by several orders of magnitude.

For $|E| \leqslant 2\sqrt{Z_2F}$:

$$\eta(\tau) = |\eta_+|\left(\frac{1 - \mathrm{cn}(\theta|m_\eta)}{\mathrm{sn}(\theta|m_\eta)}\right)^2, \tag{9a}$$

where

$$|\eta_+| = p\left(\frac{Z_2}{Z_c}\right)^{1/2}, \quad \theta = \left(\frac{Z_2}{Z_c}\right)^{1/4} x,$$

$$m_\eta = \frac{1}{2}\left[1 - \mathrm{sgn}(E)\left(\frac{Z_2}{Z_c}\right)^{-1/2}\right]. \tag{9b}$$

And finally for $E \geqslant 2\sqrt{Z_2F}$:

$$\eta(\tau) = |\eta_+|\,\frac{\mathrm{sn}^2(\psi|m_\eta)}{1 - \mathrm{sn}^2(\psi|m_\eta)}, \tag{9c}$$

where

$$|\eta_+| = p\left[1 - \left(1 - \frac{Z_2}{Z_c}\right)^{1/2}\right], \quad \psi = \frac{1}{2}\left[1 + \left(1 - \frac{Z_2}{Z_c}\right)^{1/2}\right]^{1/2} x,$$

$$m_\eta = 2\left[1 + \left(1 - \frac{Z_2}{Z_c}\right)^{-1/2}\right]^{-1}. \tag{9d}$$

The geometrical properties of the classical motion relevant to photoelectron imaging at threshold will be discussed in the following section. For the moment, let us simply outline that the classical model allows us to divide the energy range in three regions: below the saddle-point energy E_c the classical motion is bound; between the saddle-point energy and the zero-field ionization energy ($E = 0$) the motion is bound along the ξ coordinate and along the η coordinate if $\beta < \beta_c$, otherwise it is open along η if $\beta \geqslant \beta_c$; finally, for positive energy, the motion is always open along the η coordinate.

The inspection of the set of equations (5) and (9) shows that the topology of the electron trajectories, and hence of the pattern of impacts at large distance, depends only on the sign of E and on the dimensionless parameter Z_c [Eq. (5d)]. In

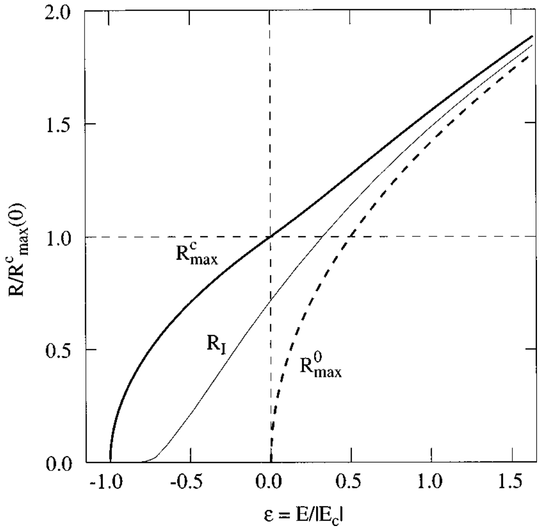

FIG. 2. Maximum radius of impact neglecting the Coulomb term $R^0_{\max}$ (dotted line) and taking the Coulomb term into account $R^c_{\max}$ (solid line) as a function of the reduced energy ε. At large ε values, $R^0_{\max}$ and $R^c_{\max}$ do not differ significantly while for $-1 \leqslant \varepsilon \leqslant 1$, the effect of the Coulomb interaction cannot be neglected.

the following, we consider only the case of photoionization of a neutral atom. In that case, $Z_1 + Z_2 = Z = 1$ and the reduced energy is simply related to Z_c by $\varepsilon = \mathrm{sgn}(E)\sqrt{Z_c}$. The parameter Z_c (or equivalently ε) is thus a measure of the relative strength of the Coulomb and Stark field. On the other hand, the actual dimension of the image depends essentially on the parameter p [Eq. (5b)] which represents the ratio between initial and final kinetic energy, and of course on L, distance between the ionization region and the detector. From Eqs. (5) and (9), we can deduce the maximum radius of the image, i.e., the maximum distance an electron can reach with respect to the center O' of the projection pattern. This radius depends on whether or not the Coulomb field is taken into account. Neglecting the Coulomb interaction (photodetachment or fast electron in photoionization) it is easy to demonstrate [31] that this maximal radius is

$$R^0_{\max} = 2(pL + p^2)^{1/2} \quad \text{for } E \geqslant 0 \tag{10}$$

while, for $E < 0$, the electron does not leave the core.

If the Coulomb interaction is taken into account, the motion is bound if $E \leqslant -2\sqrt{F}$, otherwise

$$R^c_{\max} = (-p + 2F^{-1/2})^{1/2}(2L)^{1/2} \quad \text{for } -2\sqrt{F} \leqslant E \leqslant 0, \tag{11a}$$

$$R^c_{\max} = \left[p + \left(p^2 + \frac{4}{F} \right)^{1/2} \right]^{1/2} (2L)^{1/2} \quad \text{for } E \geqslant 0. \tag{11b}$$

Equations (10) and (11) are compared in Fig. 2. $R^0_{\max}$ and $R^c_{\max}$ are plotted for ε values smaller than 2.0 together with R_I defined later. At large ε values, $R^0_{\max}$ and $R^c_{\max}$ do not differ significantly while it is clear that for $-1 \leqslant \varepsilon \leqslant 1$, the effect of the Coulomb interaction can hardly be neglected.

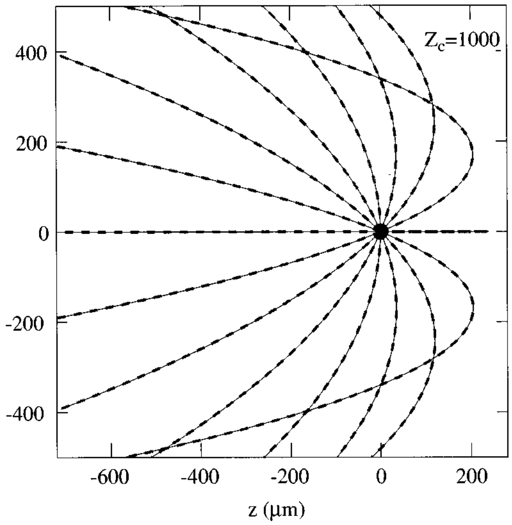

FIG. 3. Comparison between ballistic trajectories (thick dotted lines) and exact trajectories (thin solid lines) for fast electrons ($Z_c = 1000$) and various ejection angles. The following numerical values have been used: $F = 1$ V/cm, $E = 193.57$ cm^{-1}. No difference between exact and ballistic trajectories is visible. Here and in the following, the electric field F is oriented along the positive z axis.

III. PROPERTIES OF THE CLASSICAL TRAJECTORIES AND SIMULATED IMAGES

In this section we discuss the properties of the classical trajectories from different points of view. First, we compare the exact classical trajectories with those computed neglecting the influence of the Coulomb field. Then, we examine the evolution of the radius of impact of photoelectrons on a plane detector far from the ionization region as a function of the ejection angle β. On this basis, we discuss the generic properties of the classical trajectories. After this discussion, two-dimensional images obtained under various initial conditions and regimes are presented. Finally, we discuss the limitation of our calculations and how they can be compared with wave-packet quantum calculations.

A. Comparison between exact and ballistic trajectories

If one neglects the long-range Coulomb interaction, the electrons in a homogeneous electric field follow simple parabolic (ballistic) trajectories: the electron motion is equivalent to a free fall with constant acceleration. Let us first compare exact and ballistic trajectories in the case of a rather fast photoelectron. As mentioned above, the key parameter defining the nature of the trajectories, and hence the fast or slow character of the electron with respect to the external field, is the parameter Z_c (or ε). Typically, a slow electron corresponds to Z_c values in the range 0–1 ($-1 \leqslant \varepsilon \leqslant 1$), while a fast electron corresponds to values larger than 100 ($\varepsilon \geqslant 10$). In Fig. 3 both kinds of trajectories are plotted for photoelectrons ejected at various angles with $Z_c = 1000$. At the scale of the figure, no difference is visible between exact and ballistic trajectories. Under these conditions the influence of the Coulomb field may be neglected and the standard approximation used in photoelectron imaging spectroscopy applies. Note that, under experimental conditions applied so far in photoelectron imaging [29–31], Z_c values smaller than

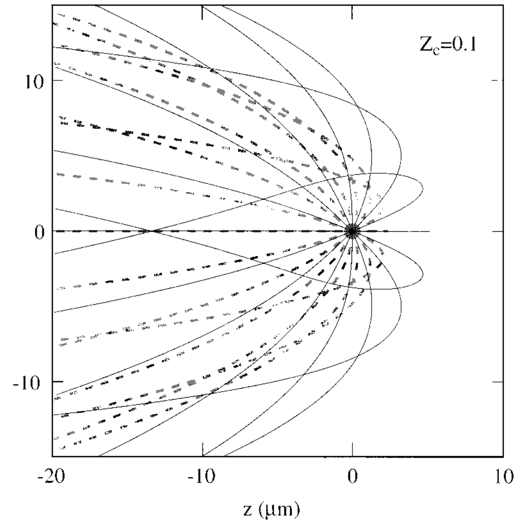

FIG. 4. Comparison between ballistic trajectories (thick dotted lines) and exact trajectories (thin solid lines) for slow photoelectrons ($Z_c=0.1$). The following numerical values have been used: $F=1$ V/cm, $E=1.936\ \mathrm{cm}^{-1}$. Exact and ballistic trajectories are totally different.

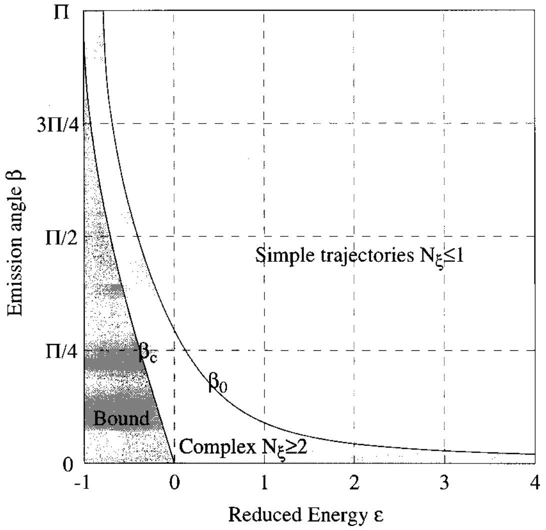

FIG. 5. Critical angles β_c and β_0 as a function of the reduced energy ε. For a given energy value, the space is divided in three distinct regions according to the ejection angle β: for $\beta<\beta_c$ the electron motion is bound and $N_\xi \rightarrow \infty$; for $\beta_c \leqslant \beta \leqslant \beta_0$ the electron motion is complex and $N_\xi \geqslant 2$; for $\beta_0 \leqslant \beta$ the electron motion is simple and $N_\xi \leqslant 1$.

1000 are seldom used. The same comparison is presented in Fig. 4 for the case of a very slow electron with $Z_c=0.1$. The exact trajectories are now extremely different from simple parabola.

In the case of a fast electron, it is only when it is ejected in a direction almost parallel to the external field (upfield) that it passes again very close to the core, thus experiencing a distorted potential and a significant scattering. This happens only at very small ejection angle β. It can be shown that for any energy value $E>E_c$ one can define a critical angle $\beta_0(\varepsilon)$ such that an electron launched with energy $E=\varepsilon|E_c|$ at $\beta_0(\varepsilon)$ falls at a distance $R=0$ from the center O' of the plane detector at ''infinite'' distance L. The evolution of the critical angle β_0 as a function of ε is shown in Fig. 5. For $\beta>\beta_0(\varepsilon)$, the classical trajectory is not significantly different from a simple parabola ($N_\xi=0$ or 1), while for $\beta<\beta_0(\varepsilon)$, significant departure from parabolic trajectory appears and the number of turning points along the ξ coordinate (N_ξ) is strictly larger than 1. As ε increases, the angle $\beta_0(\varepsilon)$ becomes infinitely small and this effect has no observable consequence. In other words, as is visible in Fig. 5, the energy range is divided in three distinct regions according to the value of the ejection angle β with respect to β_c and β_0: for $\beta<\beta_c$ the electron motion is bound and $N_\xi \rightarrow \infty$; for $\beta_c \leqslant \beta < \beta_0$ the electron motion is complex and $N_\xi \geqslant 2$; for $\beta_0 \leqslant \beta$ the electron motion is simple and $N_\xi \leqslant 1$. The particular shape of trajectories at small angles and large energy is schematized in Fig. 6 for $Z_c=1000$. Figure 6 shows that even under conditions where the Coulomb field is *a priori* negligible, the influence of the Coulomb well is not totally zero at small ejection angle.

Between the saddle-point energy and the zero-field ionization energy, the comparison with ballistic trajectories is no longer possible. In that case, according to the ejection angle β, two different regions of the space may be distinguished. For $\beta<\beta_c$, the electron is classically bound. Its motion is confined by the potential barrier and by the ''limit cycle'' which corresponds to a stable orbit as defined in Refs. [18–20]. For $\beta \geqslant \beta_c$, the electron can be ejected following a complex trajectory with a number of turning points N_ξ which decreases as β increases. Figure 7 presents such a case for $Z_c=0.1$ and an ejection angle β close to β_c.

B. Evolution of the radius of impact of photoelectrons as a function of β

From the point of view of photoelectron imaging spectroscopy, or more generally if we are interested in the properties of the electron trajectories at macroscopic distances from the atom, the relevant quantity is the distance R of impact of the electron from the center O' of the image (see

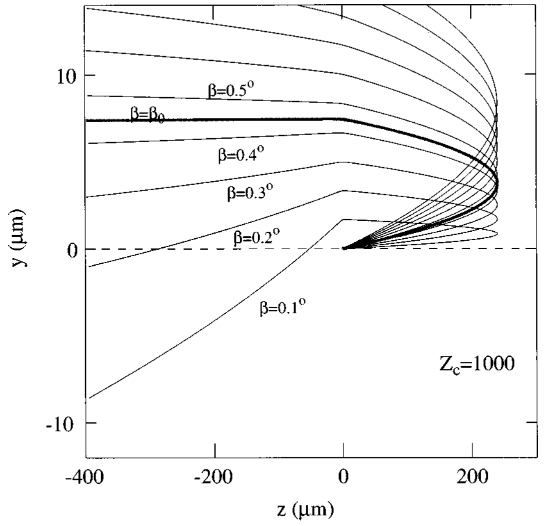

FIG. 6. Classical trajectories at small angles and large energy ($Z_c=1000$) (not to scale). In this particular case, electrons ejected at $\beta_0 \approx 0.45°$ are found, at large distance from the core, at $y=0$ ($R=0$). Below this critical value, the electron is scattered by the core.

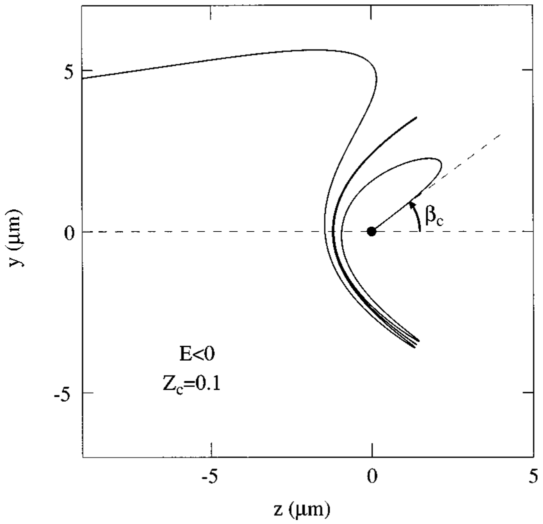

FIG. 7. Complex classical trajectory close to the critical angle β_c for $E<0$ ($Z_c=0.1$: $F=1$ V/cm, $E=-1.936\ \mathrm{cm}^{-1}$). The electron oscillates several times along the limit cycle before escaping the Coulomb attraction.

Fig. 1) as a function of the emission angle β. As mentioned above, Eqs. (5) and (9) show that the topology of the trajectories depends only on the quantity Z_c and on the sign of the energy, while the actual dimensions depend primarily on the parameter p. In other words, the overall shape of the polar plot $R(\beta)$ depends only on the value of ε, while its size depends on p. This is exactly true if the distance L between the ionization region and the detector is infinite. Under more realistic conditions where the distance L is finite, the polar representation $R(\beta)$ slightly varies with E for a given Z_c value, but this can be neglected as long as $L \gg R(\beta)$. In Fig. 8, $R(\beta)$ is plotted for $Z_c=0$, 1, 10, and 100 for positive energies, while in Fig. 9, $R(\beta)$ is plotted for negative energies and $Z_c=0.0$, 0.3, 0.6, and 0.9. Let us first discuss the case of positive energies. For large values of the parameter Z_c, the evolution of $R(\beta)$ is almost not affected by the presence of the Coulomb field, i.e., $R(\beta)\approx R_{\max}^{0}\sin(\beta)$. As Z_c decreases (see $Z_c=10$), a sharp feature peaked around $\beta=0$ appears in the polar plot $R(\beta)$. This is the manifestation of the scattering of electrons at small angles mentioned above. As Z_c decreases further, this effect becomes more and more important. For example, in Fig. 8 for low Z_c values (see $Z_c=0$) it is clearly visible that the space is divided in several regions according to the value of β: region I, downfield ($\Pi>\beta>\beta_0$), where electrons are directly ejected and follow a simple trajectory close to a parabola [first lobe in $R(\beta)$]. We define R_{I} (see Fig. 5) as the maximum value of $R(\beta)$ in this region; region II ($\beta_0>\beta>\beta_1$), where the electron is scattered once by the ionic core ($N_\xi=2$) and impacts on the detector on the side opposite to its initial emission [secondary lobe in $R(\beta)$, maximum radius $R_{\mathrm{II}}>R_{\mathrm{I}}$]; and so on with trajectories presenting an arbitrary number of turning points. In any case $R(\beta)\leq R_{\max}^{c}$ defined Eq. (11). For positive energies, it is possible to demonstrate that around $\beta=0$ there exists an infinite accumulation of lobes in $R(\beta)$, each lobe corresponding to a given N_ξ value, with an angular extension that reduces roughly with N_ξ^{-2}. This results from the metastable character of the $\beta=0$ orbit, i.e., an electron launched at $\beta=0$ stays on a finite linear orbit along the positive z axis, while an electron launched at an infinitely small angle follows a complex orbit before leaving the core (extreme sensitivity to the initial conditions). From the observation of the polar representation of $R(\beta)$ one can immediately conclude that the final image is a superposition of several rings of radius $R_{\mathrm{I}}<R_{\mathrm{II}}<\cdots<R_{\max}^{c}$ corresponding to the various lobes in $R(\beta)$. Another significant feature is that, as opposed to the case where the Coulomb field is neglected ($Z_c\rightarrow\infty$), a significant portion of electrons is emitted at $R=0$. Indeed, as already mentioned, when the Coulomb field is neglected, only electrons ejected at $\beta=0$ and Π fall on the center O' of the image at $R=0$. On the contrary when the Coulomb field is taken into account, and especially for low values of Z_c, several critical angles $\beta_i\neq 0$ and Π correspond to a central impact $R(\beta_i)=0$ ($\beta_0>\beta_1>\beta_2\cdots$). Since the total number of electrons ejected at a given angle β is proportional to $\sin(\beta)$ the relative contribution at $R=0$ increases dramatically as ε decreases (see next paragraph).

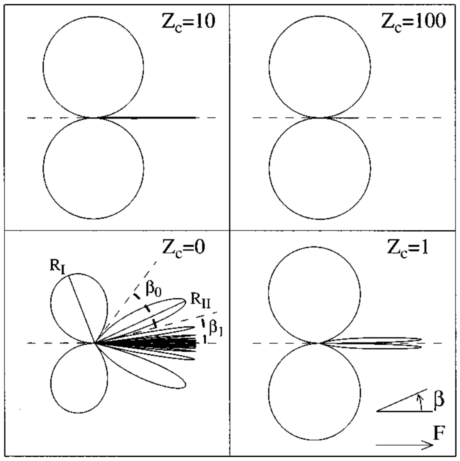

FIG. 8. Polar plot $R(\beta)$ (arbitrary units) of the radius of impact as a function of the emission angle for $Z_c=0$, 1, 10, and 100 and positive energies (see text).

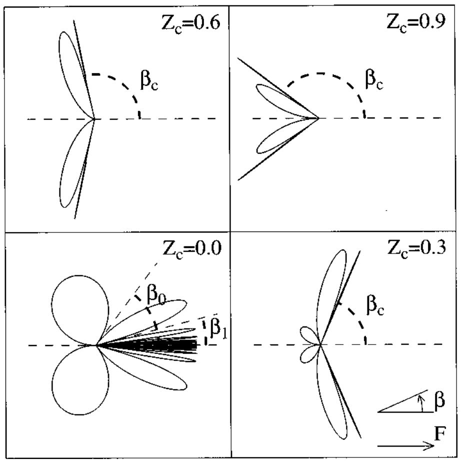

FIG. 9. Same as Fig. 8 for negative energies and $Z_c=0$, 0.3, 0.6, and 0.9.

The situation is quite different at negative energy since, in that case, one can define in addition the region of bound trajectories for $\beta<\beta_c$ where electrons cannot escape. This situation is exemplified in Fig. 9 where $R(\beta)$ is plotted for

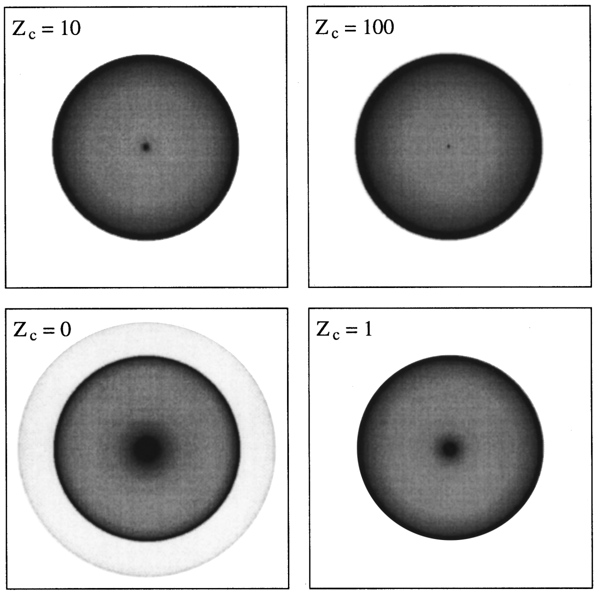

FIG. 10. Simulated images computed with an isotropic initial angular distribution and positive energies for $Z_c=0$, 1, 10, and 100. The images are scaled such that R_{I} corresponds to the same effective size. The relative number of electrons falling in a given pixel (256×256 pixel images) is represented by a gray scale ranging linearly from white (0% of maximum intensity) to black (for intensities larger than three times the minimum intensity inside the main ring).

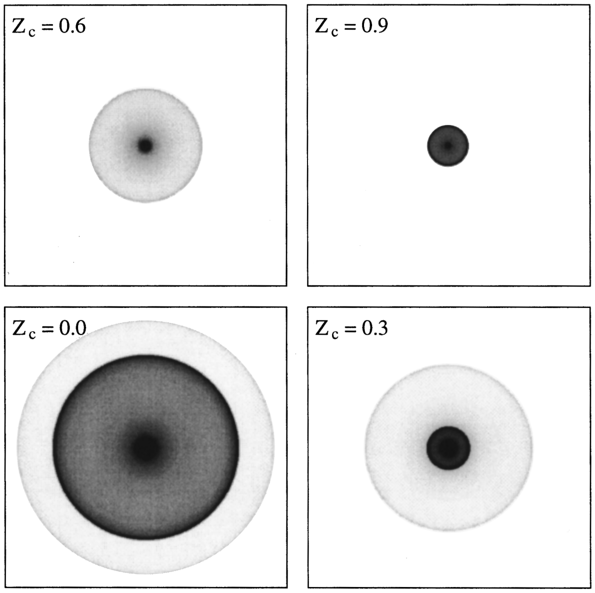

FIG. 11. Simulated images computed with an isotropic initial angular distribution $f(\Theta)=k$ and negative energies for $Z_c=0$, 0.3, 0.6, and 0.9. All images have been computed with the following actual values: $F=1$ V/cm, $L=500$ mm, dimension of the square image $D_{\mathrm{image}}=6$ mm. These values correspond to realistic experimental conditions. The truncated intensity scale is optimized in order to enhance low intensity features.

$E<0$ and $Z_c=0.0$, 0.3, 0.6, and 0.9. Similarly to the case $E>0$, the open region $(\beta>\beta_c)$ is divided in several subregions corresponding to different values of N_ξ with a primary lobe of radius R_{I} and secondary lobes of radius $R_{\mathrm{II}},\ldots,R^c_{\max}$.

C. Simulated images

The physical information obtained in a photoelectron imaging experiment is the total distribution of impacts of electron at macroscopic distance from the ionization region. This is two-dimensional information that contains both the initial kinetic energy and angular distribution. When the Coulomb field is neglected, a single energy channel W_0 corresponds to a single circular ring in the 2D image with a radius proportional to $\sqrt{W_0}$ [31]. If the Coulomb field is taken into account, the initial angular distribution $f(\Theta)$ must be combined with the $R(\beta)$ function calculated above in order to obtain a simulated image. Such images are presented in Fig. 10 for positive energies, and in Figs. 11–13 for negative energies. Let us first discuss the case of positive energies. Figure 10 presents images computed with an isotropic initial angular distribution $[f(\Theta)$ constant$]$ for $Z_c=0$, 1, 10, and 100. The images are scaled such that R_{I} corresponds to the same effective size. The relative number of electrons falling in a given pixel (256×256 pixel images) is represented by a gray scale ranging linearly from white (0% of maximum intensity) to black (for intensities larger than three times the minimum intensity inside the main ring). This truncated scale is used in order to enhance low intensity features, a full scale being not very meaningful since the maximum intensity in the central peak may be extremely high. In fact, before discretization, the signal intensity diverges at $R=0$ and at each $R_{\mathrm{I}},R_{\mathrm{II}},\ldots$ value. This divergence disappears since the image is discretized on a 256×256 grid. For the case where the electron is launched at an energy just equal to the zero-field ionization threshold $(Z_c=0)$, the image (bottom left) displays three distinct structures: a very intense and narrow central peak corresponding to the electrons emitted in the vicinity of the various angles β_i $[R(\beta_i)=0]$, an intense ring of radius R_{I} corresponding to the primary lobe, and a secondary ring of radius close to $R^c_{\max}$ corresponding to the

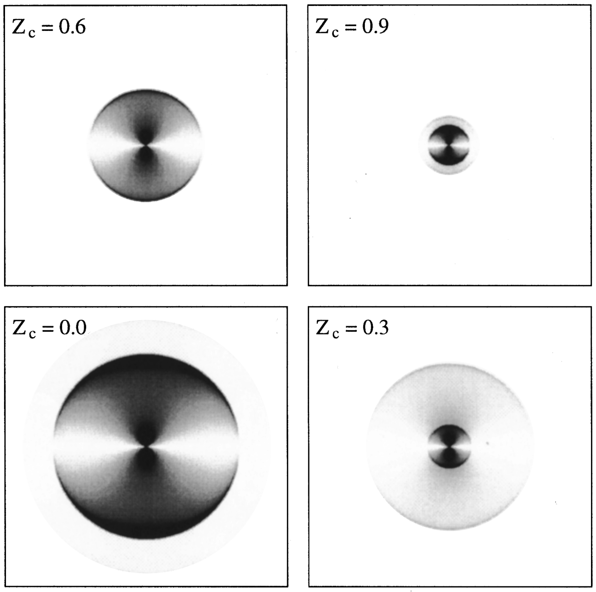

FIG. 12. Same as Fig. 11 except $f(\Theta)=k\cos^2\Theta$. The laser polarization is oriented along the vertical axis.

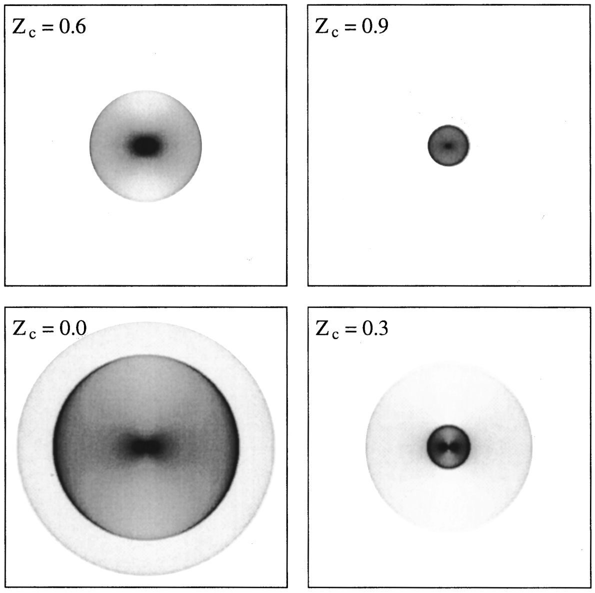

FIG. 13. Same as Fig. 12 except $f(\Theta) = k\ \sin^2\Theta$.

superposition of the other lobes. When the energy is increased significantly above the zero-field ionization threshold, the secondary ring disappears while the central peak remains $(Z_c = 1)$ although it becomes rapidly less intense $(Z_c = 10)$. At higher relative energy $(Z_c = 100)$ the central peak is practically no longer visible and we find the standard conditions of photoelectron imaging where a single ionization channel leads to a single ring of radius proportional to the initial velocity of the photoelectrons. The situation presented in Figs. 11–13 for negative energy values is more interesting and leads to a much larger variety of phenomena. These figures collect images with $Z_c = 0.0$, 0.3, 0.6, and 0.9 $(E \leqslant 0)$ for three different initial angular distributions: $f(\Theta)$ constant (Fig. 11), $f(\Theta) = k\ \cos^2\Theta$ (Fig. 12), and $f(\Theta) = k\ \sin^2\Theta$ (Fig. 13). All simulated images are computed for the same field value and represented at the same geometric scale. The intensity gray scale is optimized in order to enhance low intensity features. When the energy decreases (i.e., Z_c increases for negative energies) the ratio $R_{\mathrm{I}}/R_{\mathrm{II}} < 1$ decreases rapidly as is visible, for example, for $Z_c = 0.3$ where the inner ring is extremely intense and small as compared to the outer ring. When the energy decreases further, the primary ring progressively disappears as is visible for the case $Z_c = 0.6$ while for $Z_c = 0.9$ two separate rings are again visible. For $Z_c = 1$, the image finally reduces to a single spot. Depending on the initial angular distribution, the upfield-downfield specific features are more or less emphasized (compare Fig. 11 to 13) and the detailed structure is more or less visible. Most common angular distributions for slow photoelectrons ejected in a single photon ionization process are of the kind $f(\Theta) = k\ \cos^2\Theta$ (the electron is preferentially ejected along the laser polarization axis) and it is likely that a ‘‘real’’ experiment would lead to results qualitatively similar to those presented in Fig. 12.

According to our simulations, the most favorable region to observe the influence of the Coulomb field on the photoelectron trajectories is the region just below the zero-field ionization threshold $(E < 0)$ with Z_c in the range 0.0–0.3 where three sharply separated features are observed. Note that realistic values of the variables (E, F, L, and image size) have been used in the simulated images in order to demonstrate the feasibility of the experiment.

D. Discussion

The simulations presented above show clearly that slow electrons do not behave like fast electrons from the point of view of photoelectron imaging. Prior to the description of the various applications of the effect described above, let us briefly discuss the relevance of our classical model as compared to an exact quantum wave-packet calculation. Although an exact calculation of the pattern of impacts of photoelectrons requires a quantum description, it is well known that the motion of a quasifree electron is reasonably well described by classical trajectories. More precisely, in the case of photoionization in a weak external electric field (in order to observe significant separation between the various features) between the saddle-point energy and the zero-field ionization threshold, principal quantum numbers of the order of 100–200 are involved. Combined with the Stark effect induced by the external field, the effective density of states (resonances) is of the order of $10^4 - 10^5$ per cm^{-1}. This means that, even under high resolution and taking into account the finite width of each resonance, the optical excitation populates a superposition of states exactly described by a wave packet in time-dependent quantum mechanics. This wave packet is reasonably well described by a bunch of classical trajectories, which supports our classical model. However, as usual, classical and quantum mechanics differ radically on (at least) two points.

(i) Interferences in the projection pattern arising from the coexistence of various trajectories leading to the same position are absent from our model and the description of interference patterns such as those observed in photodetachment microscopy [28] requires a quantum (or at least semiclassical [27]) description. However, as noted above, classical mechanics works only if we are dealing with superposition of states, and in that case interferences are probably smoothed by the spreading of the wave packet. This allows us to conciliate classical and quantum approaches.

(ii) The quantum treatment of the Stark effect shows that, even above the saddle-point energy, the wave function of the excited state (or superposition of states) may be described by the parabolic quantum numbers (or a set of) $\{n_1, n_2, m_1\}$. The localization of the wave function with respect to the field orientation and hence the correspondence with the effective initial distribution versus angle β in classical mechanics is dramatic. For example, blue Stark states $\{n_1 \approx n, n_2 \approx 0, m_1\}$ which are mostly localized on the high potential side (upfield) region correspond to bunches of ‘‘classical’’ electrons launched preferentially around $\beta = 0$ while red Stark states $\{n_1 \approx 0, n_2 \approx n, m_1\}$ which are mostly localized on the low potential side (downfield) region correspond to bunches of ‘‘classical’’ electrons launched preferentially around $\beta = \Pi$. Although the classical simulation allows us to show in a very simple manner that electrons ejected around $\beta = 0$ remain longer in the vicinity of the ion which gives a simple interpretation to the longer lifetime of blue states, the asymmetric initial effective distribution which mimics the quantum wave packet and depends on both angles Θ (angle between the initial velocity $\mathbf{v}_0$ and the laser polarization) and β (angle between the initial velocity $\mathbf{v}_0$ and the external field $\mathbf{F}$) may only be included phenomenologically in the classical picture.

IV. APPLICATIONS

To summarize the classical analysis described above, we have shown that from the relative intensities and angular distributions observed in the various features contained in the image of slow electrons, one can obtain a direct measurement of various quantities that are not directly accessible by other means. Of course, slow electron imaging allows us to determine the initial kinetic energy together with the initial angular distribution but, in addition the localization of the initial wave packet (or in other words the set of parabolic quantum numbers) may be determined, at least qualitatively, as well as the effect of the scattering by the residual ion at long range (typically on a μm scale). Beside these fundamental aspects that are explicitly involved in this phenomenon, the influence of the Coulomb field and its consequences at macroscopic distances on the slow photoelectron motion may be used as a very powerful tool in order to probe the local interaction between electron(s) and ion(s) in any kind of photoionization process. On purpose, actual values corresponding to realistic situations have been used in the simulated images presented in Figs. 10–13. For example, the maximum radius of impact for $Z_c=0.0$ is about 2.5 mm with $F=1$ V/cm and a spectrometer length $L=500$ mm (see Figs. 11–13) which means that, under reasonable experimental conditions, the effect described here may be seen experimentally. Slow photoelectrons may be produced under many different experimental circumstances but schematically, one can distinguish between two categories of experiments: multiphoton ionization or autoionization involving low Rydberg states on one hand, and continuum Stark spectroscopy involving very excited states on the other hand. In both cases, it is clear that slow photoelectron imaging may provide detailed information on the fundamental processes involved. In the following, we will focus on continuum Stark spectroscopy before a brief description of the applications of slow photoelectron imaging in the area of the dynamics of field ionization and in ZEKE spectroscopy.

A. Continuum Stark spectroscopy

The spectroscopy of atomic systems in extreme values of external fields for which the motion of the excited electron is determined equally by the Coulomb field and by the external field has been a field of great interest (strong-field mixing) during recent decades. More particularly, the study of near-zero-energy resonances in atoms in an external electric field, or continuum Stark spectroscopy has been the subject of a large amount of work [32–35] and corresponds to the typical experimental situations described here $(Z_c\approx 1)$. The main feature of continuum Stark spectroscopy is the fact that, above the saddle-point energy and also above the zero-field ionization threshold, the photoionization cross section oscillates with an effective period roughly proportional to the applied external field. It has been shown [19,32,33] that this resonance structure for positive energies results from the existence of quasiperiodic classical electron orbits tightly constrained along the electric field axis (upfield). It has been shown also [35] that the maxima in the photoionization cross section arise from dominant contribution of blue Stark states $(n_1\approx n)$, while the minima correspond to a region where red Stark states $(n_1\approx 0)$ are dominant. In other words, maxima occur in the photoionization cross section when the wave function of the system, superposition of many partial waves $\{n_1,n_2,m_1\}$, is mostly localized in the upfield region (longer lifetime, sharper resonances), while minima occur when the wave function is localized in the downfield region (vicinity of the saddle point) corresponding to shorter lifetime (broader resonances). Therefore continuum Stark spectroscopy represents the typical experimental situation where the localization of the initial wave packet with respect to the Coulomb center and the field direction has a dramatic influence on the spectrum. As described in the preceding section, photoelectron imaging can provide in that case a direct (although incomplete) measurement of the probability to find the excited electron at a given ejection angle β and consequently allows a direct correlation between oscillations in the photoionization cross-section and intensity ratios between the various components of the photoelectron image that reveal the initial angular distribution as a function of β and Θ. The relative intensity of the central peak, inner ring, and outer ring is indeed directly connected to the initial distribution and it is clear that slow photoelectron imaging can lead to a significant improvement of the understanding of this regime of strong-field mixing in the continuum.

B. Dynamics

In Sec. III we have shown that many properties of the photoionization of an atom may be analyzed from a geometrical point of view. Analogous properties may also be studied in the time domain. An effect strictly equivalent (time recurrence instead of ‘‘geometrical recurrence’’) has already been observed at much higher electric field values in the time domain. Indeed, from a classical point of view within the simple formalism described in Sec. II, it is easy to show that electrons emitted downfield are ejected first, while those emitted upfield are delayed. In the experiment realized by Lankhuijzen and Noordam [36], the authors were able to show that electrons are emitted in bursts separated by a few picoseconds: those ejected downfield (large β) appearing first, those ejected upfield (small β) later. In the case of very slow photoelectrons this time scale is of course larger and falls in the nanosecond range which means that a combined time-resolved and geometrically resolved experiment is achievable. The experiment of Lankhuijzen and Noordam has been simulated by Robicheaux and Shaw [17] by calculating the propagation of a wave packet in the combined Coulomb and Stark field. However, in that case, rather small quantum numbers are involved and the quantum approach is possible, which is not trivial in the case of $n\approx 100-200$. In other words, the comparison of our results with the works of Noordam and Robicheaux shows that slow photoelectron imaging provides a geometrical approach of the dynamics of the ionization process which is very complementary to the time-evolution approach.

C. ZEKE spectroscopy and ZEKE imaging

One of the most interesting aspects of the influence of the Coulomb interaction in slow photoelectron imaging is probably its crucial importance in ZEKE spectroscopy and dynamics [25,26]. Indeed, the modification of the observed pattern for a nonhydrogenic core or as a function of the density of residual ions can reveal the local potentials involved in the dynamics of a ZEKE electron. Let us first mention briefly the microscopic lens described elsewhere [38]. In a rather different context since it concerns fast electrons of about 1 eV interacting with a few thousand residual ions (qualitatively same E/Z value) we have shown that the presence of a finite number of ions in the interaction region has visible consequences on the photoelectron image: the higher the number of charges, the sharper the effect of the perturbation in the photoelectron images. This effect has been evidenced in $3+1$ photon ionization of xenon where a thin line, parallel to the laser propagation, appears in the image when more than about 1000 Xe^+ residual ions are present in the interaction region. Now, let us imagine the situation where an electron excited in the vicinity of the saddle-point energy interacts, not only with the ion from which it has been removed, but also with other ions located at typical distances of a few tens of micrometers. If one looks at the effective potential generated by a distribution of charges of this kind (typically 10^9 charges cm^{-3} in a very small region), it is obvious that the trajectory of the electron is extremely perturbed. In particular, each positive charge in the environment of the electron increases the binding energy of the electron in the ionization region but at the same time lowers the effective saddle-point energy. A few charges instead of a single one will also severely distort the shape of the $R(\beta)$ distribution at large distance and it is not clear at all that the specific features described in Sec. III (central peak, two concentric rings) are still visible in the images when a charge distribution is present. This means that, in return, we can take advantage of this effect in order to analyze the dynamics of photoionization in the presence of distributed charges. In usual ZEKE experiments, very high-n Rydberg bound states excited just below the ionization limit are ionized by a pulsed electric field (PFI: pulsed-field-ionization) after a delay of a few microseconds, revealing the presence of a discrete level of the positive ion. It has been shown that the lifetime of such ZEKE states, and consequently the intensity of ZEKE signal, is extremely sensitive to the ion density in the photoionization region [39–41]. Strictly speaking, the process described here does not concern directly PFI-ZEKE electrons since ZEKE deals with states lying just below the saddle-point energy while the phenomenon described here appears just above the saddle point. However, the physics in this region is not essentially different for bound and continuum states and the experimental study of the influence of the density of charges on the geometrical aspect of photoionization could shed a new light on this class of phenomenon. In particular, the lengthening of the lifetime of the ZEKE states has been attributed to the breakdown of the local cylindrical symmetry induced by the distributed charges [39–41] and the subsequent loss of quantum number m_1 which is, in principle, preserved in the Stark effect. Mixing with higher m_1 values may be only a partial explanation to the lengthening of the lifetime of the ZEKE states, and an experiment based on the principle discussed here could probably show what is the respective influence of the breakdown of the spherical symmetry and of the perturbation of the classical trajectories induced by the charge distribution.

V. CONCLUSION

In this paper we have shown that imaging spectroscopy of slow photoelectron is qualitatively different from the traditional photoelectron imaging [29–31]. The structure of the projected image is more complex and the crucial point is that the strength of the various components of the image depends on the distribution of the orientation of the initial velocity of the photoelectron with respect to the electric field axis. This provides a unique tool to study the properties of the wave function of an atom excited in an external electric field, and more particularly the initial localization of the wave packet after optical excitation. Slow photoelectron imaging seems particularly appropriate to the study of continuum Stark spectroscopy and a long photoelectron imaging spectrometer, specially designed for slow electrons, is presently under construction in order to observe the effect described in Sec. III. The study of the influence of a finite distribution of charges on the trajectories of slow photoelectrons is also under way with a particular attention to its consequences in the field of ZEKE spectroscopy and dynamics.

ACKNOWLEDGMENTS

Fruitful discussions with Professor Hanspeter Helm are gratefully acknowledged. The ‘‘Laboratoire de Spectrométrie Ionique et Moléculaire’’ is a ‘‘Unité Mixte de Recherche CNRS–Université Lyon I’’ (UMR CNRS 5579).

---

[1] See, for example, H. A. Bethe and E. E. Salpeter, *Quantum Mechanics of One- and Two-Electron Atoms* (Plenum, New York, 1977).

[2] R. J. Damburg and V. V. Kolosov, J. Phys. B **9**, 3149 (1976); **11**, 1921 (1978); **12**, 2637 (1979).

[3] R. J. Damburg and V. V. Kolosov, in *Rydberg States of Atoms and Molecules*, edited by R. F. Stebbings and F. B. Dunning (Cambridge University Press, Cambridge, England, 1983).

[4] H. J. Silverstone, Phys. Rev. A **18**, 1853 (1978).

[5] G. F. Drukarev, Zh. Eksp. Teor. Fiz. **75**, 473 (1978) [Sov. Phys. JETP **48**, 237 (1978)].

[6] E. Luc-Koenig and L. Bachelier, J. Phys. B **13**, 1743 (1980); **13**, 1769 (1980).

[7] D. A. Harmin, Phys. Rev. A **24**, 2491 (1981); Phys. Rev. Lett. **49**, 128 (1982); Phys. Rev. A **26**, 2656 (1982); **30**, 2413 (1984); Comments At. Mol. Phys. **15**, 281 (1985).

[8] K. Sakimoto, J. Phys. B **19**, 3011 (1986).

[9] T. F. Gallagher, *Rydberg Atoms* (Cambridge University Press, Cambridge, England, 1994); see also *Rydberg States of Atoms and Molecules*, edited by R. F. Stebbings and F. B. Dunning (Cambridge University Press, Cambridge, England, 1983).

[10] M. L. Zimmerman, T. W. Ducas, M. G. Littman, and D.

Kleppner, J. Phys. B **11**, L11 (1978).

[11] M. L. Zimmerman, M. G. Littman, M. M. Kash, and D. Kleppner, Phys. Rev. A **20**, 2251 (1979).

[12] J. W. Cooper and E. B. Saloman, Phys. Rev. A **26**, 1452 (1982).

[13] C. Chardonnet, F. Penent, D. Delande, F. Biraben, and J. C. Gay, J. Phys. (France) Lett. **44**, L517 (1983).

[14] C. Fabre, Y. Kaluzny, R. Calabrese, L. Jun, P. Goy, and S. Haroche, J. Phys. B **17**, 3217 (1984).

[15] C. T. W. Lahaye and W. Hogervorst, Phys. Rev. A **39**, 5658 (1989).

[16] Z. Dacic Gaeta and C. R. Stroud, Jr., Phys. Rev. A **42**, 6308 (1990).

[17] F. Robicheaux and J. Shaw, Phys. Rev. Lett. **77**, 4154 (1996).

[18] J. Gao and J. B. Delos, Phys. Rev. A **49**, 869 (1994).

[19] J. Gao, J. B. Delos, and M. Baruch, Phys. Rev. A **46**, 1449 (1992).

[20] J. Gao and J. B. Delos, Phys. Rev. A **46**, 1455 (1992).

[21] J. E. Bayfield and P. M. Koch, Phys. Rev. Lett. **33**, 258 (1974).

[22] P. M. Koch and D. R. Mariani, Phys. Rev. Lett. **46**, 1275 (1981).

[23] W. R. S. Garton, W. H. Parkinson, and E. M. Reeves, Proc. Phys. Soc. London **80**, 860 (1962).

[24] W. Sandner, K. A. Safinya, and T. F. Gallagher, Phys. Rev. A **33**, 1008 (1986).

[25] K. Müller-Dethlefs, M. Sander, and E. W. Schlag, Chem. Phys. Lett. **112**, 291 (1984).

[26] K. Müller-Dethlefs and E. W. Schlag, Annu. Rev. Phys. Chem. **42**, 109 (1991); K. Müller-Dethlefs, E. W. Schlag, E. R. Grant, K. Wang, and V. McKoy, Adv. Chem. Phys. **90**, 1 (1995); E. W. Schlag and R. D. Levine, Comments At. Mol. Phys. **33**, 159 (1997).

[27] V. D. Kondratovitch and V. N. Ostrovsky, Zh. Eksp. Teor. Fiz. **79**, 395 (1980) [Sov. Phys. JETP **52**, 198 (1980)]; J. Phys. B **17**, 1981 (1984); **17**, 2011 (1984); **23**, 21 (1990); **23**, 3785 (1990).

[28] C. Blondel, C. Delsart, and F. Dulieu, Phys. Rev. Lett. **77**, 3755 (1996).

[29] H. Helm, N. Bjerre, M. Dyer, D. Huestis, and M. Saeed, Phys. Rev. Lett. **70**, 3221 (1993).

[30] C. Bordas, M. J. Dyer, T. Fairfield, H. Helm, and K. C. Kulander, Phys. Rev. A **51**, 3726 (1995).

[31] C. Bordas, F. Paulig, H. Helm, and D. L. Huestis, Rev. Sci. Instrum. **67**, 2257 (1996).

[32] R. R. Freeman, N. P. Economou, G. C. Bjorklund, and K. T. Lu, Phys. Rev. Lett. **41**, 1463 (1978).

[33] R. R. Freeman and N. P. Economou, Phys. Rev. A **20**, 2356 (1979).

[34] A. R. P. Rau and K. T. Lu, Phys. Rev. A **21**, 1057 (1980).

[35] T. S. Luk, L. DiMauro, T. Bergeman, and H. Metcalf, Phys. Rev. Lett. **47**, 83 (1981).

[36] G. M. Lankhuijzen and L. D. Noordam, Phys. Rev. Lett. **76**, 1784 (1996).

[37] V. V. Beletzky, *Essays on the Motion of Celestial Bodies* (Mir, Moscow, 1977). Note that the motion of an electron in the combined Stark and Coulomb field is strictly equivalent to the motion of a satellite under the combined effect of gravitational attraction of a planet (analogous to the Coulomb term) and of a constant acceleration (homogeneous external field).

[38] C. Bordas and J. C. Pinaré, Phys. Rev. A **57**, 681 (1998).

[39] F. Merkt and R. N. Zare, J. Chem. Phys. **101**, 3495 (1994).

[40] M. J. Vrakking and Y. T. Lee, J. Chem. Phys. **102**, 8818 (1995); **102**, 8833 (1995).

[41] M. J. Vrakking, I. Fischer, D. M. Villeneuve, and A. Stolow, J. Chem. Phys. **103**, 4538 (1995).